

Deep-Learning-Based Control of a Decoupled Two-Segment Continuum Robot for Endoscopic Submucosal Dissection

Yuancheng Shao^{*1,2}, Yao Zhang^{*3}, Jia Gu², Senior Member, IEEE, Zixi Chen⁴, Di Wu⁵, Yuqiao Chen^{2,6}, Bo Lu⁷, Member, IEEE, Wenjie Liu¹, Cesare Stefanini⁴, Member, IEEE, Peng Qi¹, Member, IEEE

Abstract—Manual endoscopic submucosal dissection (ESD) is technically demanding, and existing single-segment robotic tools offer limited dexterity. These limitations motivate the development of more advanced solutions. To address this, DESectBot, a novel dual-segment continuum robot with a decoupled structure and integrated surgical forceps, enabling 6 degrees of freedom (DoFs) tip dexterity for improved lesion targeting in ESD, was developed in this work. Deep learning controllers based on gated recurrent units (GRUs) for simultaneous tip position and orientation control, effectively handling the nonlinear coupling between continuum segments, were proposed. The GRU controller was benchmarked against Jacobian-based inverse kinematics, model predictive control (MPC), a feedforward neural network (FNN), and a long short-term memory (LSTM) network. In addition, a systematic ablation study under identical training conditions showed that, for the considered control task, the GRU achieves better generalization, faster convergence, and higher computational efficiency than the LSTM. In nested-rectangle and Lissajous trajectory tracking tasks, the GRU achieved the lowest position/orientation RMSEs: 1.11 mm/ 4.62° and 0.81 mm/ 2.59°, respectively. For orientation control at a fixed position (four target poses), the GRU attained a mean RMSE of 0.14 mm and 0.72°, outperforming all alternatives. In a peg transfer task, the GRU achieved a 100% success rate (120 success/120 attempts) with an average transfer time of 11.8 s, the STD significantly outperforms novice-controlled systems. Additionally, an *ex vivo* ESD demonstration—grasping, elevating, and resecting tissue as the scalpel completed the cut—confirmed that DESectBot provides sufficient stiffness to divide thick gastric mucosa and an operative workspace adequate for large lesions. These results confirm that GRU-based control significantly enhances precision, reliability, and usability in ESD surgical training scenarios.

Index Terms—Endoscopic Submucosal Dissection (ESD), continuum robot, learning-based control

This work is supported by the National Key Research and Development Program of China under Grant No. 2023YFB4705200, in part by the National Natural Science Foundation of China under Grant No. 62273257 and 62203315, in part by the Natural Science Foundation of Jiangsu Province of China (BK20220490), in part by the Innovation and Entrepreneurship Leading Talent Program of Suzhou City (ZXL2023156), and in part by the Young Elite Scientists Sponsorship Program by CAST (2023QNRC001). (Yuancheng Shao and Yao Zhang contributed equally to this work.) (Corresponding Author: Peng Qi and Bo Lu).

¹ Department of Control Science and Engineering, College of Electronics and Information Engineering, Tongji University, No. 1239, Siping Road, Shanghai 200092, China;

² Department of Data Science, City University of Macau, China;

³ Department of Mechanical Engineering, KU Leuven, 3000 Leuven, Belgium;

⁴ The Biorobotics Institute and the Department of Excellence in Robotics and AI, Scuola Superiore Sant'Anna, 56127 Pisa, Italy;

⁵ The Maersk Mc-Kinney Møller Institute, University of Southern Denmark, 5230 Odense, Denmark;

⁶ Surgical Robotics R&D Center, Zhuhai Institute of Advanced Technology, Zhuhai 519085, Guangdong Province, China;

⁷ The Robotics and Microsystems Center, School of Mechanical and Electric Engineering, Soochow University, Suzhou, Jiangsu, China.

I. INTRODUCTION

Gastrointestinal (GI) cancers represent a major global health burden. In 2018, an estimated 4.8 million new cases led to 3.4 million deaths, accounting for 26 % of all cancer diagnoses and 35 % of cancer fatalities worldwide [1]. These high mortality rates are driven by late-stage detection and a range of risk factors—including infections, lifestyle behaviors, and dietary habits [2]. These alarming mortality figures underscore the urgent need for progress in prevention, early diagnosis, and the development of more effective treatments to address this high-mortality challenge to public health.

Endoscopic Submucosal Dissection (ESD) has become a widely embraced clinical method for treating early-stage GI cancer, offering a significant boost to survival rates [3]. This minimally invasive surgical procedure not only minimizes patient discomfort but also facilitates faster recovery times and shorter hospital stays. In contrast to conventional endoscopic mucosal resection (EMR), ESD offers several advantages: (i) lower recurrence rates; (ii) the ability to excise lesions en bloc regardless of size, whereas EMR is confined to lesions under 20 mm; (iii) provision of optimal specimens for precise histopathological evaluation; and (iv) potential resection of lesions unsuitable for EMR [4]. However, performing ESD requires advanced technical skills and involves a higher risk of complications, necessitating years of training to master the various modalities of procedure [5].

A. Robot Assisted Endoscopy

However, traditional endoscopes face several limitations. Firstly, their limited maneuverability and precision can make it difficult to accurately target and resect early-stage cancers or precancerous lesions, particularly in the anatomically complex regions of the GI tract [6]. Secondly, the success of these procedures is contingent upon the clinician's manual dexterity and critical decision-making, which contributes to variability in ESD outcomes [7]. Lastly, most endoscopes are still manually controlled, which places a significant physical strain on physicians during lengthy ESD procedures. This can result in fatigue, decreased precision, and potentially compromise the treatment's success. Therefore, to address the aforementioned issues, or at least some of them, researchers have introduced robotics technology into the endoscopy procedure.

To mitigate potential patient harm and access lesions deep within the body through natural orifices, research on soft and flexible continuum surgery instruments has gained significant traction [8]. [9] introduced a transendoscopic flexible parallel continuum robotic mechanism with a miniature wrist for ESD treatment. However, single-segment robotic endoscopes have limited flexibility and range of motion, and they also struggle to maintain stable visualization. This becomes particularly

problematic in complex areas of the GI tract, such as the esophago-gastric junction. This region, where the esophagus meets the stomach, features a sharp angle and tight space, making it challenging to access and resect lesions with a single-segment endoscope due to its limited maneuverability [10]. Achieving and maintaining a direct line of sight for precise dissection can be difficult. Furthermore, manipulating instruments for cutting and coagulation without compromising the visual field or risking injury to surrounding tissues poses a significant challenge, increasing the likelihood of incomplete resection or perforation.

To address the aforementioned challenges, the development of multi-segment robotic endoscopes has been investigated. Compared to the single-segment robot, the multi-segment robot has advantages with more DoFs and higher distal dexterity [11]. In the context of ESD treatment, multi-segment robotic endoscopes show promising capabilities for precise execution of surgical steps, including multi-angle cutting operations relative to lesion surfaces and efficient en-bloc resection. Notably, a two-segment robotized soft endoscope incorporated with two calibrated cameras demonstrated feasibility for ESD treatment [12]. Moreover, our previous work introduced a dual-segment robotic platform, DESEctBot, featuring a spatial cross-curved disk skeleton structure and showed promising trajectory tracking performance. However, the multi-segment structure introduces increased nonlinearities, and the need for more actuators to control each segment adds complexity to control.

B. Deep Learning Based (DL-based) Control of Continuum Robot

Deep learning (DL) methods are highly valued in the control of continuum robots due to their ability to model complex and non-linear dynamics and use data to improve precision and accuracy. DL-based algorithms could continuously refine control strategies for improved performance, particularly in applications requiring intricate manipulation, such as minimally invasive procedures. To precisely control tendon-driven robots, the Recurrent Neural Network (RNN) method is proposed to address the non-linear and non-repeatable elastic behavior [13]. Furthermore, two DL methods, Multilayer Perceptron (MLP) and RNN, were utilized to predict the distal-end force of tendon-sheath mechanisms in flexible endoscopic surgical robots [14]. To model hysteresis and other nonlinearities in flexible continuum robots, both Long Short-Term Memory (LSTM) and Gated Recurrent Unit (GRU) networks—two memory-based recurrent architectures—have been explored. LSTM was first used to predict distal-tip responses and, in a subsequent study, embedded in a feed-forward controller to compensate for hysteretic behavior in free and constrained motions [15], [16]. More recently, GRU networks have likewise been implemented to control multi-DOF articulated soft robots, demonstrating comparable efficacy for handling non-linear, hysteretic dynamics [17], [18]. Furthermore, a combination of DL methods and an online optimization kinematics controller was proposed to further reduce the errors caused solely by the neural network controller [19]. However, as of now, DL methods have yet to be utilized in the control of two-segment endoscope robots. Consequently, this paper seeks to leverage DL techniques to address the nonlinear phenomena in the DESEctBot system and further achieve precise control of the robot, showcasing the potential for advanced DL techniques to enhance robotic endoscopy.

C. Main Contributions and Paper Structure

To the best of our knowledge, this is the first paper to leverage a recurrent-based deep learning method on a two-segment endoscopic robot for challenging tasks such as simultaneous position and orientation control, which is required by surgery such as endoscopic submucosal dissection.

The main contributions of this paper are:

- A novel dual-segment continuum robot DESEctBot with an integrated surgical forceps end effector was established for ESD.
- Implement a proposed data-driven method to model the inverse kinematics of DESEctBot, from which a DL-based Gate Recurrent Unit (GRU) controller has been established. Validation of the position and orientation control precision of DESEctBot integrated with GRU, by comparing several model-based and data-driven methods, through benchtop experiments.
- Carry out the benchmark peg transfer test by GRU-driven DESEctBot and make a performance comparison with a well-known surgical robot which confirms its suitability for standardized ESD skill training.

The structure of this paper is outlined as follows: Section II details DESEctBot's hardware and kinematics. Section III presents the GRU-based controller and data collection, contrasting model-based and learning approaches. Section IV reports trajectory-tracking and dexterity tests. Section V evaluates a benchmark peg-transfer task and *ex vivo* ESD demonstration. Section VI concludes and outlines future work.

II. SYSTEM DESIGN

Commercial multifunctional tools such as marking needles for submucosal injection, mucosal incision knives, electrosurgical dissection knives and hemostatic devices are widely used [20], yet they generally lack full six DoFs capability. This shortfall hinders precise lesion targeting and accurate tooltip orientation while maintaining endoscope stability within the gastrointestinal lumen [21]. As a result, clinicians must undergo extensive training to execute these complex maneuvers safely and effectively [22], and inadequate control can lead to tissue injury, perforation or bleeding [23]. It is therefore essential to develop ESD instruments with true 6 DoFs dexterity in order to meet clinical demands for lesion access and shorten the learning curve, reduce procedure time and enhance surgical safety [24].

The overall DESEctBot system addresses these requirements by providing 6 DoFs via four integrated modules: an actuation module (encompassing translation and rotation) enclosed by an exterior cover, a passive bending module, a double active bending module (DABM) and a custom-designed end effector.

1) *DESEctBot actuation module*: The actuation module consists of seven DC motors (ECXSP16L, Maxon Motor AG, Switzerland) equipped with GPX16HP (44:1) gearboxes. These motors are divided into three groups: a drive motor unit, a rotation motor, and a translation motor. All motors are controlled by a multi-axis motion controller (P-MASONON, Elmo Motion Control Ltd, Israel). The drive motor unit includes five DC motors, each connected to a coupling and cable fixing slider blocks. Using a lead screw and nut mechanism, the rotational motion of the DC motors is converted into the linear motion of the sliders. These sliders are arranged in a regular pentagon along the central axis. Four sliders actuate the double active bending module via nickel-titanium (NiTi)

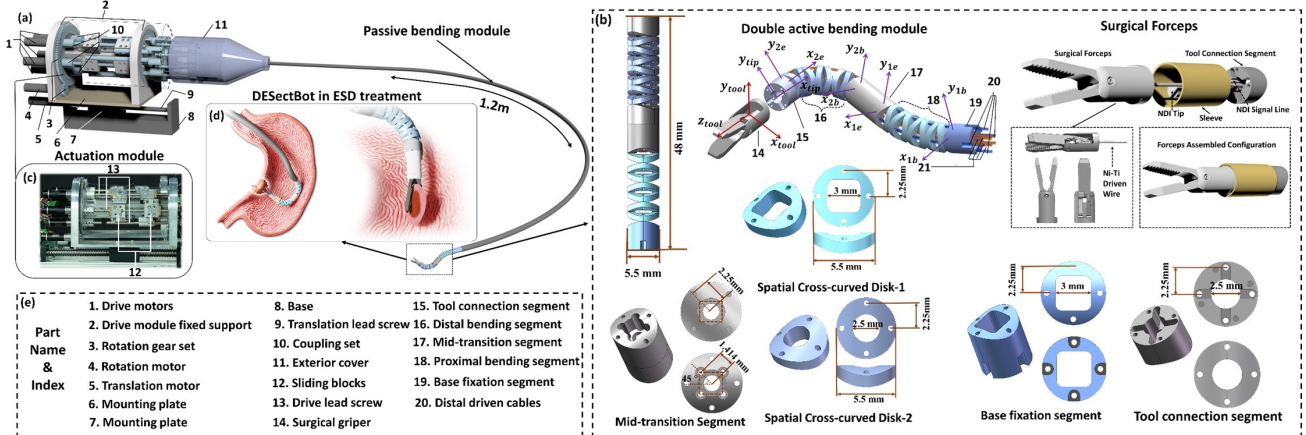


Fig. 1: Decoupled Endoscopic Submucosal Dissection Robot (DESectBot): (a) detailed assembly drawing of DESectBot system, (b) detailed parts drawing of double active bending module with surgical gripper in kinematics coordinate system, (c) DESectBot actuation module, (d) demonstration of DESectBot in ESD treatment, (e) part name and corresponding index

tendons (ϕ 0.5 mm), while the remaining slider drives the surgical tool. The entire actuation module can rotate and translate via the rotation and translation motors, respectively. The module is enclosed in a 3D-printed exterior cover, which is easily disassembled for maintenance.

2) *DESectBot passive bending module*: The passive bending module is made of ebonite and has a standard length of 1.2 meters. NiTi tendons are threaded through this sheath structure.

3) *DESectBot DABM*: As shown in Fig. 1 (b), the DABM consists of a proximal and a distal bending segment connected by a rigid mid-transition segment. Each segment is actuated by NiTi tendons, allowing it to bend independently in isolation. The mid-transition link mechanically decouples the two segments, so bending one segment minimally affects the other. Both bending segments utilize a dual continuum manipulator mechanism based on spatial cross-curved disk (SCD) joints: a skeletal element permitting continuous multi-directional bending. The proximal segment uses an SCD-1 joint skeleton and the distal segment uses SCD-2. Each SCD disk has two perpendicular curved slots, forming a cross-curved structure that permits multi-directional bending. In the proximal segment, tendon guide holes are evenly spaced (every 90°), whereas in the distal segment they are rotated by 45°. With two pairs of opposing tendons per segment, this SCD-based structure enables full 3D bending of both segments. Stacking the disks in alternating orientations (each pair rotated 90° relative to the next) yields a cross-arc configuration that allows the DABM to bend in four orthogonal directions with minimal inter-segment coupling.

4) *Surgical Forceps End Effector*: In this study, as shown in Fig. 1(b) a surgical forceps with 5mm diameter and 20mm length was designed and integrated as the DESectBot's end effector at the distal tip of the DABM. The forceps attaches via a custom 6.5mm-diameter, 15mm-long sleeve and incorporates a compact antagonistic NiTi cable-driven mechanism for precise tissue manipulation. One 6 DoFs electromagnetic (EM) tracker (Aurora V3.1, Northern Digital Inc., Canada) tip is embedded in the tool segment to provide real-time tip pose feedback. The surgical forceps assembly is modular, allowing quick replacement and sterilization between procedures. When coupled with DABM, the integrated forceps achieve enhanced dexterity and control, enabling simultaneous yet decoupled control of position and orientation. The decoupling mechanism

TABLE I: Quantitative summary of drift, normalized hysteresis, and motion stroke under repeated cyclic loading

Load (g)	Mean Drift (mm)	Norm. Hysteresis Area	Mean Stroke (mm)
0	0.41	0.0119	13.40
50	0.46	0.0134	11.16
100	0.47	0.0152	9.72

between the proximal and distal segments is detailed in previous work [25], where it was shown that the unintended motion (crosstalk) between the segments is minimal, with angular deviations of less than 1°, confirming effective decoupling. This capability overcomes the limited dexterity and orientation control of conventional ESD instruments, simplifying ESD procedures and improving lesion-targeting precision and tissue manipulation.

5) *Hysteresis Analysis*: Because DESectBot relies on multiple NiTi tendons routed through a long passive bending module, hysteresis, friction, and load-dependent drift are inherent to the tendon-sheath mechanism. These effects were analyzed through controlled cyclic actuation experiments under different external loading conditions, confirming predictable and non-divergent behavior under repeated loading and unloading. To mitigate these effects, the system design and control framework incorporate tendon pre-tensioning, low-friction sheath routing. Regarding clinical translation, the distal tool and tendon-sheath assembly are based on biocompatible NiTi components compatible with standard sterilization methods, while motors and electronics remain outside the sterile field, supporting integration into conventional clinical workflows.

III. ROBOT CONTROL METHODS

In view of the fact that the DESectBot is a two-segment continuum robot system, it is a challenge to simultaneously control the position and orientation of the DABM tip to perform the ESD tasks. Therefore, two model-based control methods, three data-driven neural networks, were established here for DABM. Furthermore, the characteristics of these methods detailed analysis shown in Table II.

A. Jacobian Kinematic Control

The kinematic model of the DABM has already been derived under the constant-curvature assumption in our earlier work [25]. In that formulation, each continuum segment is parameterised by the bending-angle vector $\Psi_i = [\theta_i, \delta_i]^T$.

θ_i and δ_i , and closed-form expressions for the forward and differential kinematics were obtained.

The present study builds on that foundation by incorporating the distal surgical forceps tool, which was not included in the previous model, and by developing the corresponding kinematics control strategies. From Fig. 1 (b) and Eq. (6) in [25], the representation matrix of the tool frame $\{tip\}$ relative to the base frame $\{1_b\}$ is:

$$T_{tool}^{1_b} = T_{tip}^{1_b} T_{tool}^{tip} = T_{1e}^{1b} T_{2b}^{1e} T_{2e}^{2b} T_{tip}^{2e} T_{tool}^{tip}. \quad (1)$$

Then attach a fixed forceps frame $\{tool\}$ with a tool length d_t at the tip via

$$T_{1_b}^{tip} = \begin{bmatrix} I_3 & p_{tool} \\ \mathbf{0} & 1 \end{bmatrix}, \quad p_{tool} = \begin{bmatrix} 0 \\ 0 \\ d_t \end{bmatrix}, \quad (2)$$

Analogous to the continuum inverse kinematics (Eq. (5)-(7) in [25]), the instantaneous kinematics of the full DESectBot system is:

$$\dot{X}_{tool} = J_{\Psi_{tool}} \dot{\Psi}_{tool} \quad (3)$$

Where $J_{\Psi_{tool}}$ is the Jacobian matrix of the entire continuum manipulator with forceps derived from J_{Ψ_i} .

B. Model Predictive Control

In the design of closed-loop model-based controllers for DeSectBot, Model Predictive Control (MPC) theory can be applied to cable-driven continuum robot to achieve optimal system inputs at each moment [26]. The proposed nonlinear model predictive control method utilizes predictions of future outputs during the modeling stage to determine the current system's optimal input. The model input is determined through a target optimization function, and this predictive model does not require multiple sensors to gather the posture of the continuum arm. It relies solely on the predicted time-series outputs to achieve precise and stable pose control of the DeSectBot.

According to model prediction theory, under given target trajectory pose X_r , conditions, the optimal input u of the system at each control moment can be obtained by solving the optimal solution of the objective function. The objective function and constraint conditions are as follows:

$$M(k) = \sum_{i=k}^{N+k} e^T(k) Q e(k) + \sum_{i=k}^{N+k} \Delta u^T(k) P \Delta u(k), \quad (4)$$

$$e(i) = X_r(k) - X(k), \quad (5)$$

$$X(k) = X(k-1) + J(u) \Delta u(k-1), \quad (6)$$

where N is the predicted time domain, J represent the Jacobian matrix, Δu is the change in system input, Q and P are diagonal weighing matrices, the optimal solution of the objective function can be obtained to achieve the current system input u and minimize pose error.

C. Data-Driven Inverse-Kinematics Networks

An alternative approach employs purely data-driven networks that learn a direct mapping from measured tip errors to actuator commands. Three architectures are examined in this work: feed-forward neural networks (FNN), long short-term memory (LSTM) networks, and gated recurrent units (GRU).

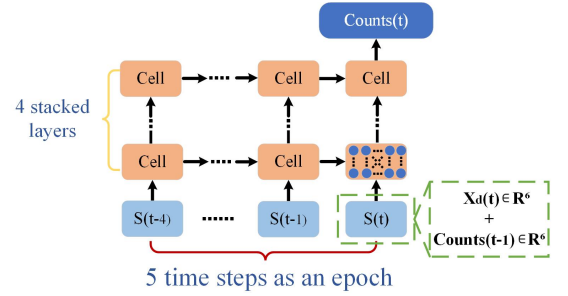


Fig. 2: Internal GRU neural network structure for robot control: a 4 stacked layers GRU that is composed of multiple GRU cells. Five time steps are taken as the input epoch, and each time step state S size is 12, which contains the target pose at the moment t and the actual motor rotation counts from the previous moment $t-1$. In this work, each cell consists of 128 neurons, and the overall network is used to predict the motor rotation counts (t).

1) *Feed-forward neural network (FNN)*: A feedforward neural network (FNN) is a static, memoryless model that learns to directly map recent state histories to current control commands [27], [28]. In this work, the FNN takes as input a fixed window of the last N tip error vectors for both continuum segments

$$\mathbf{E}_{k-N:k-1} = [\mathbf{e}(k-1)^\top, \dots, \mathbf{e}(k-N)^\top]^\top \in \mathbb{R}^{6N}, \quad (7)$$

where each $\mathbf{e}(i) \in \mathbb{R}^6$ concatenates the positions and orientation errors of dual-segments at time i , and outputs the required actuator increments for each segment at the current time step

$$\Delta\theta(k) = \mathcal{F}_{\text{FNN}}(\mathbf{E}_{k-N:k-1}) \in \mathbb{R}^4, \quad (8)$$

which indicates the vector of increases in motor angle for the four tendon actuators (two per segment) at time k .

2) *LSTM network*: To capture long-range, nonlinear interactions, the standard LSTM cell [15] with input, forget and output gates—stacked in 4 layers of 128 units, was implemented. In the proposed LSTM controller, an input sequence of the past robot states,

$$S_{t-T:t-1} = \{X(t-T), u(t-T), \dots, X(t-1), u(t-1)\}, \quad (9)$$

is used to predict the motor rotation counts at the time t , where $X(t)$ denotes the six-dimensional pose (position and orientation) of the DABM tip and $u(t)$ the corresponding motor commands.

3) *GRU Controller*: The gated recurrent unit (GRU) is a memory-based neural network that captures the temporal characteristics of robot dynamics and is adopted here for DESectBot pose control. Figure 2 depicts the computations performed inside a single GRU cell [17], [29]:

$$\begin{aligned} z(t) &= \sigma(W_z S(t) + U_z h(t-1) + b_z), \\ r(t) &= \sigma(W_r S(t) + U_r h(t-1) + b_r), \\ \tilde{h}(t) &= \tanh(W_h S(t) + U_h (r(t) \odot h(t-1)) + b_h), \\ h(t) &= (1 - z(t)) \odot h(t-1) + z(t) \odot \tilde{h}(t). \end{aligned} \quad (10)$$

where $S(t), h(t), z(t), r(t), \tilde{h}(t)$ represent the input vector, output vector, update gate vector, reset gate vector, and candidate activation vector for this unit. W_*, U_* , and b_* represent input weight, output weight, and bias parameters for each vector, which will be learned during training.

During training, the GRU receives the 12-dimensional input vector

$$\mathbf{S}_*(t) = [\mathbf{X}_d(t)^\top, \mathbf{u}(t-1)^\top]^\top \in \mathbb{R}^{12}, \quad (11)$$

TABLE II: Comparison of Control Methods for Two-Segment Continuum Robots

Controller	Method Type	Memory	Dual-Segment Mechanism Support	Advantages	Disadvantages
Jacobian	Model-based	None	Basic: per-segment		Sensitive to theoretical model error
MPC	Model-based	None	Medium: includes multi-segment constraints	Low latency; Anticipates future states; Fast inference and training	Limited by model fidelity
FNN	Data-driven	None	Low: no temporal memory; coupling only via data	Captures long-term dependencies; Lightweight; faster inference	Static mapping; lacks adaptivity
LSTM	Data-driven	Long-term	High: learns inter-segment coupling		Slower inference
GRU	Data-driven	Mid-term	High: coupling learning with reduced complexity		Slightly reduced memory vs. LSTM

TABLE III: Hyperparameter tuning of GRU and LSTM structure

Hidden layers number / Structure	Hidden size	Validation loss	Training time per epoch (s)
3 / GRU	64	0.1164	3.6331
3 / LSTM	64	0.1380	5.1216
4 / GRU	128	0.0501	5.0039
4 / LSTM	128	0.1092	7.0134
5 / GRU	256	0.0507	5.2529
5 / LSTM	256	0.1165	7.4827

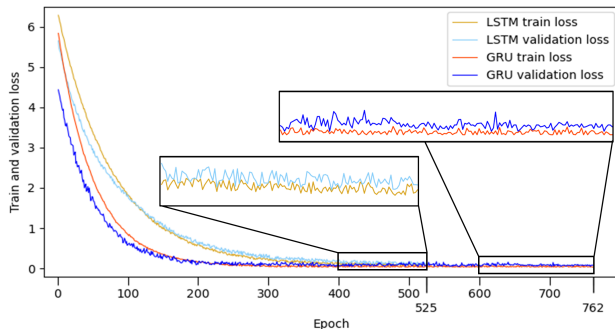


Fig. 3: Training and validation loss curves of GRU and LSTM models as a function of training epochs.

which concatenates the six DoFs tip pose $\mathbf{X}_d(t)$ with the six motor-rotation counts $\mathbf{u}(t-1)$. The learning target is the current motor-rotation vector

$$\mathbf{h}_*(t) = \mathbf{u}(t) \in \mathbb{R}^6. \quad (12)$$

At run time the pose term $\mathbf{X}_d(t)$ is replaced by the desired tip pose, following the scheme described in [19].

TABLE IV: GRU & LSTM HYPERPARAMETER

Parameter	Value	Parameter	Value
Layer Number	4	Input Size	12
Output Size	6	Previous Time Step	5
Hidden State Size	128	Batch Size	64
Optimizer	Adam	Learning Rate	0.001
Loss Function	L2 Loss	Epochs Number	1500

D. Data Acquisition and Training

The hardware experimental setup comprises three main components: the DESEctBot platform, support brackets, and a 6 DoFs NDI® EM tracker. As depicted in Fig. 4, four support brackets were installed to maintain the horizontal orientation of the DESEctBot passive bending module. This setup accounts for the length of the module and natural sagging, ensuring smooth transmission of the actuation force from the actuation module to the DABM. Furthermore, the NDI® EM sensor tracker tip is affixed to the central hole of the tool connection segment within the DABM, with its predefined local coordinate system.

The input and output mapping for the acquisition of GRU data are the DABM tip pose and its corresponding motor rotation counts. The general samples to train the GRU model are obtained using a Monte Carlo method, all training data trajectories are randomly generated and mapped with motor rotation counts on each time pin within a 4080 second duration, ensuring that the DESEctBot can obtain sufficient training data for various situations to deal with multiple operable tasks

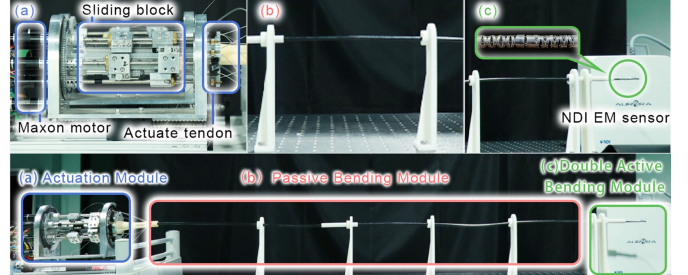


Fig. 4: Experimental hardware setup for data acquisition, position, and orientation control. *Bottom*: (a) the DESEctBot actuation module, (b) passive bending module with four support brackets to maintain its horizontal orientation, (c) double active bending module. *Top*: all parts are local close-up enlargements of the *Bottom* section. (a) shows detailed structure of actuation module, (b) intercepts a section of the passive bending module and zooms in on the details, (c) shows the detailed structure of DABM and the white square object is the NDI® EM sensor equipment which its tracker tip is affixed to the central hole of the tool connection segment within the DABM.

and fall within a single safe working time at the same time. The NDI sensor measures position and orientation with respect to the local coordinate system at a rate of 5 Hz, summing to a sample size of 20400 and its training, validation and test sets are 14280, 4080 and 2040 respectively. All data-driven models were trained on the identical dataset using same computing hardware condition (8 GB NVIDIA® RTX 4060Ti GPU).

To determine whether the observed performance advantage of the GRU arises from architectural suitability rather than hyperparameter bias, a compact ablation study was conducted by systematically varying the recurrent architecture (GRU vs. LSTM), the number of hidden units 64,128,256, and the number of layers 3,4,5 under identical training conditions. All models shared the same input–output dimensions, number of time steps, optimizer, learning rate, and batch size. Early stopping was applied based on the validation MAE with a patience of 10 epochs.

As summarized in Table III, the GRU consistently achieved lower validation loss than the LSTM across all tested configurations. The best-performing model was a four-layer GRU with 128 hidden units, which yielded the lowest validation loss of 0.0501 while maintaining favorable computational efficiency. Shallower GRU models exhibited insufficient representational capacity, whereas deeper or wider configurations did not provide additional performance gains, indicating an optimal bias–variance trade-off at moderate depth. The LSTM followed a similar trend, with its best performance also achieved using four layers and 128 hidden units (validation loss 0.1092). However, LSTM models consistently exhibited higher validation loss and longer per-epoch training times, and increasing network depth or hidden size did not improve generalization. Fig. 3 compares the learning curves of the best-performing GRU and LSTM models. While both architectures converge stably, the LSTM shows slower convergence, a larger generalization gap, and earlier termination due to early stopping (epoch 525), whereas the GRU continues improving until

epoch 762. The complete set of evaluated hyperparameters is summarized in Table IV. Overall, these results indicate that for the short-horizon temporal dynamics considered in this study, the GRU architecture provides a more effective balance between model capacity, generalization performance, and computational efficiency. All tip-tracked data collected during the Monte Carlo sampling process are confined within the designed dome-shaped DABM workspace of $\phi 60 \times 45 \text{ mm}$ (circular area \times height), which defines the coverage of the training dataset. The evaluation trajectories (Fig. 5) are defined within a smaller sub-region of $40 \times 30 \text{ mm}$ (outermost edge) and two 15 mm-amplitude loop Lissajous curves which are entirely excluded from the training data.

IV. EXPERIMENTS

To validate the proposed controller described in Section III, a benchtop experimental setup was established. Two kinds of trajectories and one set of orientation control experiments designed to closely mimic the clinical requirements of ESD procedures were implemented to assess the performance of the proposed GRU controller.

A. Experimental setup and calibration

A comprehensive experimental setup—matching the hardware and communication architecture used during data acquisition (Section III)—was built to evaluate the controllers under realistic surgical conditions. In brief, the DESEctBot system comprises:

- A seven-motor actuation module (Maxon ECXSP16L with GPX16HP gearboxes), split into five tendon-drive motors, one rotation motor, and one translation motor.
- A 1.2 m ebonite sheath serving as the passive bending module, supported by four custom brackets.
- A DABM with two 18 mm continuum segments constructed from spatial cross-curved disks, each actuated by antagonistic NiTi tendons.
- A 6 DoFs electromagnetic tracker (NDI® Aurora V3.1) mounted on the DABM tip provides real-time 5 Hz measurements of position and orientation within the robot's workspace.

The Control software is hosted on a dedicated PC, and the model-based controller was developed in C++ and interfaces directly with the Maxon motor controllers through the manufacturer's Controller Area Network-based API. This low-level implementation achieves submillisecond command latency and deterministic cycle times.

In contrast, learning-based data-driven controllers are developed in Python, leveraging PyTorch for neural network inference. To bridge between the Python environment and the C++ motor drivers and facilitate the testing of the algorithm model, a lightweight REST API using Flask was deployed:

- **Flask server (Python):** Listens on TCP port for JSON-encoded control requests; decodes desired pose, runs the GRU forward pass, and returns motor increment commands.
- **C++ client:** Uses the standard `Httpplib` library to asynchronously POST target poses to the Flask endpoint, parse the returned motor commands, and send them to the actuation module.

Both controllers run at 5 Hz, synchronized via a dedicated LAN switch. Control commands travel on an isolated TCP/IP network to minimize jitter, while a separate UDP link carries

an emergency-stop signal that shuts the motors down within 2 ms if communication fails or safety is triggered. The mean actual inference time (in milliseconds) for each controller (Jacobian 11.37 ms, MPC 17.45 ms, FNN 5.02 ms, LSTM 12.63ms, and GRU 8.91ms) on the deployment hardware, providing a practical comparison of computational efficiency.

To standardize every trial, the fixed NDI planar field generator defines the global frame. After each run, an auto-reset script zeroes motor counts, thereby returning the end effector close to its zero pose. The Elmo Application Studio II (64-bit) interface was used to increment each motor encoder in ± 500 -count steps. Real-time pose feedback from NDI ToolBox (v5.000.019) guided successive adjustments until the end-effector error was reduced to within $\pm 0.5 \text{ mm}$ in position and $\pm 0.3^\circ$ in Euler orientation—values matching the sensor's root mean square error (RMSE) accuracy (0.48 mm and 0.3° , respectively). All timestamps and poses are logged, a custom GUI streams live configuration and errors, and a model-based optimizer is being developed to replace the current manual fine-tuning.

B. Position and orientation control

This section benchmarks the five controllers from Section III against the two kinematic goals most relevant to endoscopic work—precise Cartesian positioning and accurate end-effector orientation.

To mimic typical intra-luminal motions, two path-tracking tasks were chosen. A Lissajous curve represents the smooth arcs used for marking and circumferential cutting, while a nested-rectangle path captures the straight-line advances required for submucosal dissection and tissue lifting [9]. Each controller performed five runs on both trajectories, allowing a fair comparison of accuracy, repeatability, and robustness.

1) **Nested Rectangle:** The nested-rectangle path consists of concentric rectangles connected by straight segments. As shown in Fig. 5(a), the tip first translates 15 mm along the +Y axis to reach the target plane. It then completes a rectangular loop; after each lap, the rectangle is enlarged by 5 mm on every side until the outermost loop measures $40 \text{ mm} \times 30 \text{ mm}$. During tracking, the NDI sensor samples the tip pose at 5 Hz, while the DABM keeps its orientation fixed along +Y.

As shown in the Fig. 5 (a), the GRU-based controller yields the tightest clustering around the ground truth path, indicating superior trial-to-trial consistency. Quantitatively, for the nested-rectangle task, GRU attains MAE of 0.57 mm (X), 0.45 mm (Y) and 0.62 mm (Z) (Table V), representing reductions of roughly 5 % in X and 4 % in Y compared to LSTM (0.60 / 0.47 mm) and over 15 % compared to MPC (0.68 / 0.60 mm). While the GRU attains a marginally higher MAE in the Z-direction (0.62 mm versus 0.61 mm for the LSTM), it comprises only 350208 trainable parameters—approximately 75% of the LSTM's 466944—thereby reducing computational overhead and yielding faster inference. Furthermore, the standard deviation (STD) of all position errors indicates the GRU enhanced robustness and consistency and can achieve more stable and repeatable tracking performance.

In orientation tracking the GRU posts MAEs of 1.59° (X), 2.99° (Y) and 2.12° (Z), representing approximately 12 %, 8% and 7% gains over LSTM ($1.80^\circ / 3.25^\circ / 2.28^\circ$). MPC edges the GRU on two isolated metrics—orientation-X MAE (1.43°) and orientation-Y STD (0.82°)—yet the GRU prevails elsewhere, yielding the lowest positional errors on every axis, the smallest orientation-Z spread, and the best overall RMSE

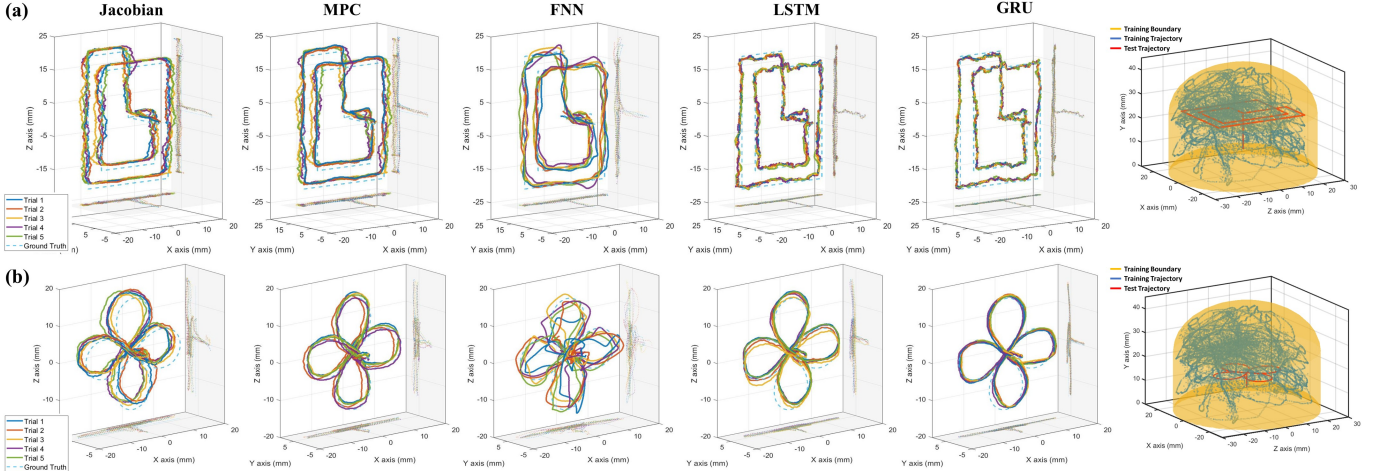


Fig. 5: Trajectory experiment: (a) Three-dimensional visualization of the five trials for each controller motion trajectory with one ground truth nested rectangle trajectory, (b) Three-dimensional visualization of the five trials for each controller motion trajectory with one ground truth lissajous trajectory. The yellow designed dome-shaped volume indicates the training data collection workspace which has a dimension of $\phi 60 \times 45 \text{ mm}$ (circular area \times height), within which all training trajectories were sampled before. The red curve represents the experimental test trajectory, excluded from the training set and used solely for performance evaluation.

TABLE V: DATA ANALYSIS OF TASK A

Nested Rectangle								
Controller	Pos X (mm)	Pos Y (mm)	Pos Z (mm)	MAE STD	Ori X (°)	Ori Y (°)	Ori Z (°)	RMSE
Jacobian	0.93	0.73	1.47	0.62	1.23	0.43	3.14	1.59 5.87 1.68 4.34 2.19 2.38 9.70
MPC	0.68	0.14	0.60	0.17	1.31	0.26	1.43	1.18 3.12 0.82 2.50 1.96 1.89 4.98(98)
FNN	0.76	0.69	0.60	0.63	0.73	0.64	2.85	2.05 4.42 1.94 2.77 2.97 1.50 6.80
LSTM	0.60	0.34	0.47	0.27	0.61	0.33	1.80	1.26 3.25 1.36 2.28 1.98 1.13 4.98(76)
GRU	0.57	0.10	0.45	0.11	0.62	0.15	1.59	1.15 2.99 1.05 2.12 1.17 1.11 4.62

Lissajous								
Controller	Pos X (mm)	Pos Y (mm)	Pos Z (mm)	MAE STD	Ori X (°)	Ori Y (°)	Ori Z (°)	RMSE
Jacobian	1.00	0.91	1.22	0.53	0.96	0.25	4.74	1.94 6.34 1.50 3.81 2.02 1.61 6.86
MPC	0.87	0.53	0.64	0.63	0.84	0.47	0.52	0.43 3.21 0.96 3.11 1.65 1.19 3.80
FNN	1.02	1.09	0.78	0.83	1.05	1.11	2.39	2.15 4.00 1.74 2.68 2.21 1.58 4.52
LSTM	0.60	0.20	0.49	0.38	1.00	0.55	0.49	0.36 2.58 0.38 2.51(03) 0.48 1.07 2.65
GRU	0.58	0.34	0.38	0.07	0.62	0.19	0.42	0.17 2.56 0.28 2.50(61) 0.24 0.81 2.59

($RMSE_{pos} = 1.11 \text{ mm}$, $RMSE_{ori} = 4.62^\circ \text{ mm}$). For comparison of RMSE, LSTM records 1.13 mm/4.99°, MPC 1.89 mm/4.99°, and the Jacobian 2.38 mm/9.70°. Hence, across the nested rectangle task, the GRU offers the highest spatial precision and repeatability among all controllers evaluated.

2) **Lissajous:** Because curved motions dominate endoscopic work and are harder to control than straight lines, all five controllers on a Lissajous path were tested [9]. The reference consists of two 15 mm-amplitude loops—one in Z, one in X—centered at the same point. Starting 6 mm above the X-Z plane, the DABM tip completes the vertical loop first and then transitions smoothly into the horizontal loop. Throughout tracking, DESectBot updates its pose at 5 Hz while keeping the end-effector oriented along +Y. As shown in Fig. 5 (b) and quantified in Table V, the GRU controller outperforms all other methods on the Lissajous path, posting the lowest values for both MAE and STD. It attains the lowest positional RMSE of 0.81 mm and orientational RMSE of 2.59°, outperforming LSTM (1.07 mm/ 2.65°), MPC (1.19 mm/ 3.80°) and the Jacobian baseline (1.61 mm/ 6.86°). These results demonstrate that the GRU adaptation effectively compensates for nonlinear coupling in the dual-segment continuum, yielding superior tracking fidelity under clinically realistic curved trajectories.

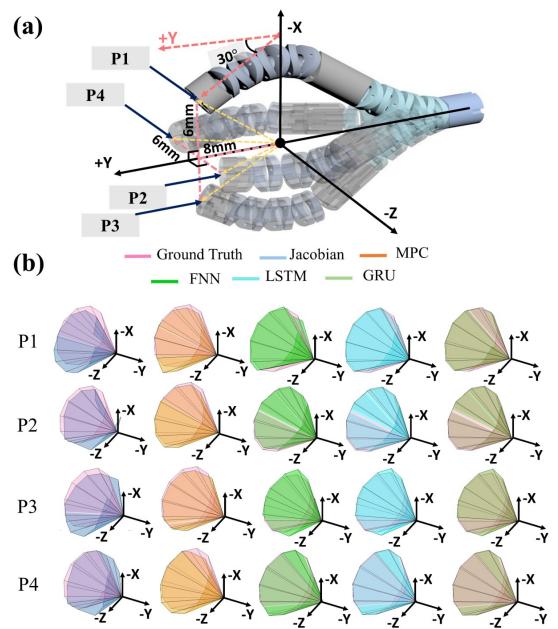


Fig. 6: (a) The DABM configuration for orientation control with four fixed tip positions P1-P4, (b) Reconstruction of orientation control experiment: a swept area that extends into a cone with a vertex angle of 30°.

TABLE VI: DATA ANALYSIS OF TASK B

Tip Points	Controller	MAE STD								RMSE		
		Pos X (mm)	Pos Y (mm)	Pos Z (mm)	Ori X (°)	Ori Y (°)	Ori Z (°)	Pos(mm)	Ori(°)			
P1	Jacobian	0.79	0.16	0.68	0.35	1.40	0.29	5.98	1.52	5.59	1.43	6.57
	MPC	0.45	0.08	0.41	0.15	0.55	0.13	2.80	0.53	3.05	0.69	3.49
	FNN	0.46	0.12	0.58	0.17	0.39	0.15	3.35	1.03	2.80	1.27	3.52
	LSTM	0.24	0.06	0.33	0.08	0.21	0.06	1.83	0.46	1.40	0.39	1.95
	GRU	0.23	0.04	0.32	0.07	0.18	0.08	1.66	0.34	1.26	0.30	1.78
P2	Jacobian	1.20	0.28	0.82	0.34	1.24	0.40	6.31	1.61	6.53	1.20	6.75
	MPC	0.41	0.09	0.30	0.05	0.46	0.09	2.16	0.45	2.12	0.63	2.70
	FNN	0.65	0.39	0.60	0.45	0.63	0.47	2.06	0.69	3.26	0.75	2.08
	LSTM	0.31	0.05	0.21	0.09	0.25	0.20	1.16	0.31	1.24	0.52	1.60
	GRU	0.27	0.03	0.18	0.08	0.22	0.02	0.99	0.28	1.07	0.30	1.38
P3	Jacobian	0.95	0.23	0.85	0.28	0.65	0.33	6.64	1.29	6.12	1.47	6.79
	MPC	0.52	0.17	0.30	0.22	0.51	0.25	2.43	0.61	2.77	0.68	4.30
	FNN	0.23	0.33	1.04	0.25	1.43	0.29	1.80	0.79	3.37	1.02	5.24
	LSTM	0.20	0.11	0.38	0.10	0.45	0.07	0.96	0.40	1.75	0.65	1.95
	GRU	0.17	0.07	0.26	0.06	0.26	0.02	0.70	0.13	0.78	0.32	1.20
P4	Jacobian	0.75	0.19	0.39	0.23	0.22	0.25	5.15	1.08	4.70	1.15	5.01
	MPC	0.50	0.28	0.35	0.11	0.47	0.12	2.26	0.37	2.25	0.53	2.50
	FNN	0.54	0.15	0.28	0.12	0.28	0.15	1.42	0.49	1.69	0.69	2.01
	LSTM	0.49	0.07	0.18	0.10	0.25	0.05	1.17	0.38	1.39	0.57	1.66
	GRU	0.45	0.09	0.17	0.07	0.23	0.06	1.10	0.26	1.29	0.44	1.54

C. Orientation control with fixed tip position

In ESD the instrument tip must stay anchored on the lesion while its orientation is repeatedly adjusted to execute complex maneuvers within a cramped, shifting workspace [10]. To evaluate this capability, experiments that rotate the DABM about a fixed DESEctBot tip position were conducted. As depicted in Fig. 6 (a), four fixed tip positions of the DABM are defined and labeled as: $P1 (-6, 8, 0)$; $P2 (0, 8, -6)$; $P3 (6, 8, 0)$; $P4 (0, 8, 6)$.

At each position, the orientation of the DABM tip is set at an angle of 30° relative to the Y -axis. Subsequently, the position of the DABM tip remains fixed, while its orientation rotates incrementally by 30° around the Y -axis. This rotation results in a swept area that extends into a cone with a vertex angle of 30° .

Figure 6 (b) presents a comparison between the ground truth and the average orientation reconstruction (all five controllers were repeated five times orientation control on each point). To clearly demonstrate the difference between the ground truth and the performance of the five controllers in each frame, every 30° step is taken as one sample for reconstruction. Table VI illustrates the MAE, STD and RMSE for positions (mm) and orientation (°), after combining it with Figure 6 (b), it is evident that in all four position scenarios, the overlap between the ground truth (pink) and the LSTM (cyan) and GRU controller (green) surfaces are the most significant compared to the other controllers. The quantitative analysis illustrates that the GRU controller markedly outperforms both model-based and alternative data-driven approaches in terms of both positional and orientational accuracy for all tests in MAE. In addition, for the vast majority of pose cases, the GRU achieved the minimum STD, demonstrating its excellent robustness in orientation control. Averaged across the four test points (P1–P4), GRU achieves the mean RMSE of 0.14 mm in position and 0.72° in orientation, compared with 0.17 mm/ 0.96° for LSTM, 0.435 mm/ 1.24° for FNN, 0.24 mm/ 1.46° for MPC, and 0.49 mm/ 3.14° for the Jacobian method. Notably, the GRU controller reduces positional RMSE by approximately 18 % relative to LSTM and by 36 % relative to MPC, while orientation RMSE is lowered by 25 % and 51 %, respectively.

The results demonstrate that the GRU effectively models the nonlinear, time-varying coupling between the two continuum segments, achieving the highest spatial accuracy and repeatability. Consequently, a GRU-driven DESEctBot provides sub-millimetric positioning and precise orientation control, making it well suited for clinical ESD tasks and confirming its superior kinematic registration and control in a two-segment continuum robot.

V. PEG TRANSFER BENCHMARK AND *Ex Vivo* EVALUATION

As demonstrated in Section IV, the proposed GRU controller delivers superior kinematic registration and control accuracy in both position and orientation. Consequently, the DESEctBot equipped with the GRU algorithm will be employed for the subsequent surgical task evaluations.

The peg-transfer task is a well-established, standardized exercise within surgical skills curricula [30] and is frequently adopted in endoscopic submucosal dissection (ESD) studies for benchmarking and training purposes [31]. In the present work, a unilateral peg-transfer protocol—executed with a single robotic arm—was implemented. Following the definitions in [32]- [33]:

- **Pick:** the DESEctBot grasps a block and lifts it clear of its initial peg.
- **Transferring:** while maintaining the grasp, the block is conveyed to the designated target peg.
- **Place:** the block is accurately deposited onto the target peg.

Compared with the aforementioned experiments, this test was utilized as a real-time input rather than predetermined trajectories. The pose of the DABM tip in each frame was controlled by a 6 DoFs master haptic interface (Sigma.7, Force Dimension AG, Switzerland), allowing for real-time adjustments. The DESEctBot teleoperation scheme is shown in Fig. 7.

A rectangular base measuring $80 \text{ mm} \times 40 \text{ mm}$ was fabricated with three parallel rows of pegs, each peg 2.25 mm in diameter. Pegs are spaced 10 mm apart along the longitudinal (Z) axis, while the transverse (X) spacing alternates between

TABLE VII: Unilateral Peg-Transfer Task Experiments

Type	Operator	Mean Transfer Time (s)	Success / Attempts	STD for Per Transfer (s)	Success Rate (%)
dVRK [33]	9 volunteers	12.3	610/636	12.90	95.9
dVRK [33]	1 surgeon	4.7	120/120	1.73	100.0
IDCM [34]	10 volunteers	15	10/10	N/A	100.0
GRU-driven DESEctBot	6 volunteers	11.8	120/120	3.93	100.0

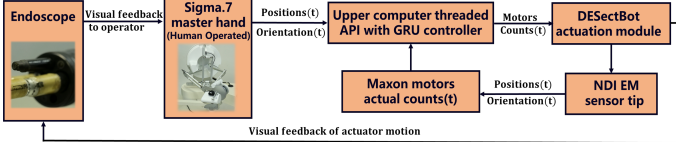


Fig. 7: The brief teleoperation scheme of DESEctBot alongside an endoscope with Sigma.7 master hand , the Motors Counts(t) represents this time step predicted motor counts for actuation module.

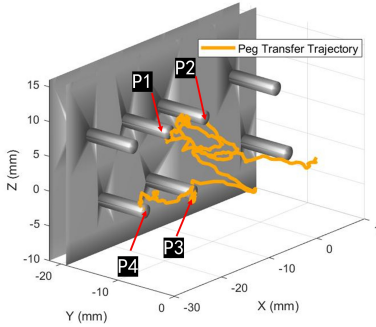


Fig. 8: Peg transfer trajectory visualization: the movement of the fastest trajectory process as an example

7.5 mm and 10 mm. Each trial comprised four sequential transfers. Six volunteer participants with no previous surgical experience were recruited; each completed a 15-minute familiarization session prior to formal testing. After system calibration and commissioning, DESEctBot was evaluated in a unilateral peg-transfer task. Figure 8 depicts the fastest trajectory recorded, and Figure 9 illustrates a representative trial:

- 1) **Pick 1:** From A(1) to A(2), the robot approaches peg P₁ and grasps the block with its forceps.
- 2) **Transfer 1 / Place 1:** From A(2) to B(1), the block is conveyed to peg P₂ and released.
- 3) **Pick 2 / Transfer 2 / Place 2:** From B(2) to B(3), the block is retrieved from P₂ and deposited on peg P₃.

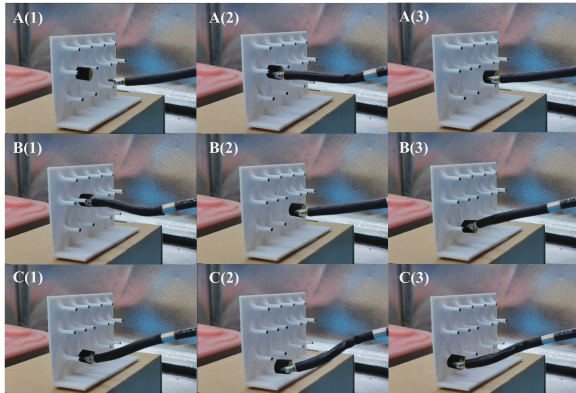


Fig. 9: A complete process including four peg transfers: DABM grasps the block at P₁ (A(1)→A(2)), transfers and releases it at P₂ (A(2)→B(1)), then moves and places it at P₃ (B(2)→B(3)), and finally conveys it to P₄ (C(1)→C(3))

- 4) **Pick 3 / Transfer 3 / Place 3:** From C(1) to C(3), the block is lifted from P₃ and placed on the final peg P₄.

Each four-move sequence constitutes one complete peg-transfer cycle for analysis, and three potential error sources were considered: (1) any systematic bias in the GRU controller should average out over the 120 transfers performed by each participant, preserving the validity of relative success-rate and timing comparisons. Second; (2) because every volunteer operates on the same hardware—and repeatability tests confirm consistent peg clearances—the influence of peg-placement tolerances and the accuracy of the NDI sensor itself is minimal; (3) the mean communication delay between the master device and DESEctBot is under 40 ms, which is significantly lower than the 200 ms (5 Hz) control interval used during evaluation. This confirms that the reported control frequency is not limited by communication latency, but rather by the EM tracking system employed exclusively for trajectory recording and ground-truth comparison.

For benchmarking, the well-established da Vinci Research Kit (dVRK) and the inverted dual continuum mechanism (IDCM) robot [33], [34] were selected as reference systems. From [33], the mean transfer time is defined as the overall completion time divided by the number of blocks. Furthermore, the STD for per transfer time is 3.93s, which significantly outperforms the novice-controlled dVRK systems. The GRU-driven DESEctBot completed the peg-transfer task faster than volunteers using the dVRK (11.8 s vs 12.3 s) while raising the success rate from 95.9% to a perfect 100%. Relative to volunteers on the IDCM platform, its 11.8 s mean time is 21.3% faster (15 s vs 11.8 s) with the same flawless success (Table VII), demonstrating both superior efficiency and reliability without requiring expert operators.

The combination of sub-12-second completion times and zero failures indicates that the GRU-driven DESEctBot delivers reliable and reproducible performance in the peg-transfer task, supporting its suitability as a standardised platform for ESD skill training.

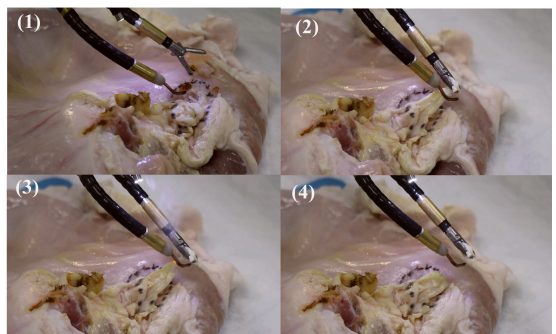


Fig. 10: *Ex vivo* evaluation of DESEctBot during a simplified ESD procedure on porcine gastric mucosa: (1) positioning; (2) grasping and lifting; (3)→(4) cutting

Furthermore, to assess DESEctBot's manipulation capabilities under real clinical settings, an *ex vivo* trial, in which porcine gastric mucosa was dissected, was conducted. In light

of the differing actuator and control mechanisms between the electro-coagulation scalpel and the forceps, a simplified ESD scenario was established, wherein most of the mucosa was pre-excised along the designated margin using the scalpel. The overall cutting duration is 403 s. Figures 10 (1)-(4) illustrate the grasping, elevating, and finally resecting of the tissue by DESEctBot as the scalpel completes the cut, which are the key steps in the ESD procedure. The successful sequence confirms that the robot provides sufficient stiffness to divide thick gastric mucosa and an adequate workspace to address lesions.

VI. CONCLUSION AND FUTURE WORK

In this paper, a novel dual-segment continuum robot with an integrated surgical forceps end effector named DESEctBot was established. For simultaneously control the DABM tip position and orientation, two model-based and three data-driven methods including the proposed GRU were established. The GRU controller consistently outperformed with Jacobian, MPC, FNN, and LSTM method in all trajectory tracking experiments. On a nested-rectangle path, GRU attained mean positional RMSE ≤ 0.17 mm and orientational RMSE $\leq 0.96^\circ$, representing improvements of all over the methods. For a complex Lissajous trajectory, GRU achieved 0.81 mm positional and 2.59° orientational RMSE, also surpassing all other methods and demonstrating its ability to compensate for dual-segment continuum nonlinearities. Moreover, in the orientation control with four fixed tip position experiment, the GRU controller markedly outperforms both model-based and alternative data-driven approaches in terms of positional and orientational accuracy and repeatability.

Building on this, a GRU-driven peg-transfer benchmark yielded a 100% success rate (120/120) with an average transfer time of 11.8 s and STD for per transfer time 3.93s, outperforming novice use of the dVRK and matching state-of-the-art continuum systems (IDCM: 15 s, 100% success), supporting suitability for standardized ESD skills training. Furthermore, an *ex vivo* demonstration on porcine gastric mucosa—grasping, elevating, and resecting the tissue while the scalpel completed the cut (total 403 s)—confirmed that DESEctBot provides sufficient stiffness to divide thick mucosa and an operative workspace adequate to address lesions. This cutting duration is comparable to reported values in robotic ESD systems (e.g., 570 s in [9]) and lies well within the range of clinically reported ESD procedure times, which typically span several tens of minutes depending on lesion size and complexity [35].

Current limitations include the control update rate used during experimental evaluation, which was constrained by the EM tracking system integrated for ground-truth measurement rather than by the control or communication pipeline itself. In future work, higher control frequencies will be pursued through the integration of faster pose-sensing modalities (e.g., next-generation EM or alternative sensing technologies) and further optimization of the control and communication pipeline, including inference acceleration and real-time software integration. In parallel, the integration of haptic and shape sensing for enhanced feedback, real-time self-calibration to compensate for tendon hysteresis and encoder drift, and the recruitment of professional surgeons for standardized comparative studies are foreseen. In addition, explicit workspace coordination and collision avoidance between the continuum robot and the endoscope will be investigated to mitigate potential workspace conflicts in multi-instrument ESD scenarios.

Additional intelligent assistance through image-based lesion detection and motion scaling, together with comprehensive preclinical animal trials, will further advance DESEctBot toward robust clinical translation.

In the near future, the integration of haptic and shape sensors for enhanced feedback for DESEctBot and real-time self-calibration to compensate for tendon hysteresis and encoder drift will be focused on. In parallel, the recruitment of additional professional surgeons is foreseen to enable more standardized comparative assessments. Moreover, intelligent assistance through image-based lesion detection and motion scaling will also be explored and undertake comprehensive preclinical animal trials to validate performance under realistic ESD conditions. These developments will advance DESEctBot toward robust clinical translation and broaden its applicability.

REFERENCES

- [1] M. Arnold *et al.*, “Global burden of 5 major types of gastrointestinal cancer,” *Gastroenterology*, vol. 159, no. 1, pp. 335–349, 2020.
- [2] A. Hormati *et al.*, “Gastrointestinal and pancreaticobiliary cancers: a comprehensive review on epidemiology and risk factors worldwide,” *Middle East Journal of Digestive Diseases*, vol. 14, no. 1, p. 5, 2022.
- [3] S. Oka *et al.*, “Advantage of endoscopic submucosal dissection compared with emr for early gastric cancer,” *Gastrointestinal endoscopy*, vol. 64, no. 6, pp. 877–883, 2006.
- [4] A. I. Kotzov *et al.*, “How to master endoscopic submucosal dissection in the usa,” *Digestive Endoscopy*, vol. 31, no. 1, pp. 94–100, 2019.
- [5] A. Y. B. Teoh *et al.*, “Difficulties and outcomes in starting endoscopic submucosal dissection,” *Surgical endoscopy*, vol. 24, pp. 1049–1054, 2010.
- [6] M. Fujishiro, “Perspective on the practical indications of endoscopic submucosal dissection of gastrointestinal neoplasms,” *World Journal of Gastroenterology: WJG*, vol. 14, no. 27, p. 4289, 2008.
- [7] X. Zhang *et al.*, “Learning curve for endoscopic submucosal dissection with an untutored, prevalence-based approach in the united states,” *Clin. Gastroenterology and Hepatology*, vol. 18, no. 3, pp. 580–588, 2020.
- [8] X. Gu and H. Ren, “A survey of transoral robotic mechanisms: Distal dexterity, variable stiffness, and triangulation,” *Cyborg and Bionic Systems*, vol. 4, p. 0007, 2023.
- [9] H. Gao *et al.*, “Transendoscopic flexible parallel continuum robotic mechanism for bimanual endoscopic submucosal dissection,” *The Int. J. of Robot. Res.*, vol. 43, no. 3, pp. 281–304, 2024.
- [10] T. W. Rice *et al.*, “Esophagus and esophagogastric junction,” *AJCC cancer staging manual*, vol. 8, pp. 185–234, 2017.
- [11] J. Burgner-Kahrs, D. C. Rucker, and H. Choset, “Continuum robots for medical applications: A survey,” *IEEE Transactions on Robotics*, vol. 31, no. 6, pp. 1261–1280, 2015.
- [12] J. Chen *et al.*, “A robotized soft endoscope with stereo vision for upper gastrointestinal endoscopic submucosal dissection (esd),” in *2023 45th Annual International Conference of the IEEE Engineering in Medicine & Biology Society (EMBC)*. IEEE, 2023, pp. 1–6.
- [13] K. Choi *et al.*, “A hybrid dynamic model for the ambidex tendon-driven manipulator,” *Mechatronics*, vol. 69, p. 102398, 2020.
- [14] X. Li *et al.*, “Distal-end force prediction of tendon-sheath mechanisms for flexible endoscopic surgical robots using deep learning,” *Mechanism and Machine Theory*, vol. 134, pp. 323–337, 2019.
- [15] D. Wu *et al.*, “Hysteresis modeling of robotic catheters based on long short-term memory network for improved environment reconstruction,” *IEEE Robot. and Automat. Lett.*, vol. 6, no. 2, pp. 2106–2113, 2021.
- [16] D. Wu, X. T. Ha *et al.*, “Deep-learning-based compliant motion control of a pneumatically-driven robotic catheter,” *IEEE Robotics and Automation Letters*, vol. 7, no. 4, pp. 8853–8860, 2022.
- [17] H. Schäfke *et al.*, “Learning-based nonlinear model predictive control of articulated soft robots using recurrent neural networks,” *IEEE Robotics and Automation Letters*, 2024.
- [18] F. Feng, W. Hong, and L. Xie, “A learning-based tip contact force estimation method for tendon-driven continuum manipulator,” *Scientific Reports*, vol. 11, no. 1, p. 17482, 2021.
- [19] Z. Chen *et al.*, “A hybrid adaptive controller for soft robot interchangeability,” *IEEE Robotics and Automation Letters*, vol. 9, no. 1, pp. 875–882, 2023.
- [20] J. T. Maple *et al.*, “Endoscopic submucosal dissection,” *Gastrointestinal endoscopy*, vol. 81, no. 6, pp. 1311–1325, 2015.
- [21] D. R. Kohli and J. Baillie, “How endoscopes work,” in *Clinical gastrointestinal endoscopy*. Elsevier, 2019, pp. 24–31.
- [22] M. X. Ma and M. J. Bourke, “Endoscopic submucosal dissection in the west: Current status and future directions,” *Digestive Endoscopy*, vol. 30, no. 3, pp. 310–320, 2018.

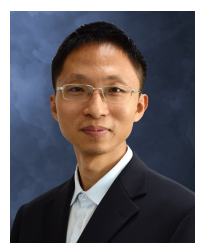
- [23] Y. Misumi and K. Nonaka, "Prevention and management of complications and education in endoscopic submucosal dissection," *Journal of Clinical Medicine*, vol. 10, no. 11, p. 2511, 2021.
- [24] N. Simaan *et al.*, "Medical technologies and challenges of robot-assisted minimally invasive intervention and diagnostics," *Annual Review of Control, Robotics, and Autonomous Systems*, vol. 1, pp. 465–490, 2018.
- [25] W. Liu *et al.*, "Desectbot: Design and validation of a novel two-segment decoupled continuum robotic system for endoscopic submucosal dissection," in *2024 IEEE/RSJ International Conference on Intelligent Robots and Systems (IROS)*. IEEE, 2024, pp. 6983–6989.
- [26] J. L. Chien, L. T. L. Clarissa, J. Liu, J. Low, and S. Foong, "Kinematic model predictive control for a novel tethered aerial cable-driven continuum robot," in *2021 IEEE/ASME International Conference on Advanced Intelligent Mechatronics (AIM)*. IEEE, 2021, pp. 1348–1354.
- [27] Y. Wang *et al.*, "Using neural networks to model hysteretic kinematics in tendon-actuated continuum robots," in *2024 International Symposium on Medical Robotics (ISMР)*. IEEE, 2024, pp. 1–7.
- [28] Y. Wang, C. Zhu, Y. Ding, B. Feng, and K. Xu, "Feedforward neural network assisted configuration transition control of continuum surgical manipulators," in *2021 27th International Conference on Mechatronics and Machine Vision in Practice (M2VIP)*. IEEE, 2021, pp. 617–622.
- [29] S. Yao *et al.*, "An rnn-lstm enhanced compact and affordable micro force sensing system for interventional continuum robots with interchangeable end-effector instruments," *IEEE Transactions on Instrumentation and Measurement*, vol. 72, pp. 1–11, 2023.
- [30] A. M. Derossis *et al.*, "Development of a model for training and evaluation of laparoscopic skills," *The American journal of surgery*, vol. 175, no. 6, pp. 482–487, 1998.
- [31] I. Habaz *et al.*, "Adaptation of the fundamentals of laparoscopic surgery box for endoscopic simulation: performance evaluation of the first 100 participants," *Surgical Endoscopy*, vol. 33, pp. 3444–3450, 2019.
- [32] S. Seung *et al.*, "Single-port robotic manipulator system for brain tumor removal surgery: Siromans," *Mechatronics*, vol. 26, pp. 16–28, 2015.
- [33] M. Hwang *et al.*, "Automating surgical peg transfer: Calibration with deep learning can exceed speed, accuracy, and consistency of humans," *IEEE Transactions on Automation Science and Engineering*, vol. 20, no. 2, pp. 909–922, 2022.
- [34] Z. Wu *et al.*, "Design of a modular continuum-articulated laparoscopic robotic tool with decoupled kinematics," *IEEE Robotics and Automation Letters*, vol. 4, no. 4, pp. 3545–3552, 2019.
- [35] C.-Y. Ko *et al.*, "Clinical outcomes of endoscopic submucosal dissection for colorectal neoplasms: A single-center experience in southern Taiwan," *Plos one*, vol. 17, no. 10, p. e0275723, 2022.



Yuancheng Shao (Student Member, IEEE) received the M.Sc. degree in human and biological robotics from Imperial College London in 2021. From 2022 to 2023, he was a medical robot motion planning and control algorithm engineer at the Advanced Technology Institute of Suzhou. He is currently working toward a Ph.D. degree at the City University of Macau in the SIAT-CityU Macau Joint Laboratory. His current research interests include medical robotics and surgical automation techniques.



Yao Zhang received the M.Sc. degree in medical technology and engineering from the Technical University of Munich, Munich, Germany in 2021. He is currently working toward the Ph.D. degree with Katholieke Universiteit Leuven, Leuven, Belgium. His research interests include novel sensing, robot control, and machine learning in medical robotics.



Jia Gu (Senior Member, IEEE) is now working with City University of Macau as a full professor and Ph.D. advisor. He received the Ph.D. degree in 2005 from University of Rennes (France). Since 2008, he has joined Chinese Academy of Sciences as a full professor, and then the deputy director of Advanced Technology Institute of Suzhou. His research interests focus on Image-Guided Instruments and Medical Robotics.



Xixi Chen (Graduate Student Member, IEEE) received the M.Sc. degree in control systems from Imperial College in 2021. He is currently pursuing the Ph.D. degree in biorobotics from Scuola Superiore Sant'Anna of Pisa. His research interest includes optical tactile sensors and soft robot control with neural networks.



Di Wu received the PhD degree in 2023 through a joint program between KU Leuven, Belgium, and Delft University of Technology, Netherlands, under the Marie Skłodowska-Curie Actions of the European Union Horizon 2020. He is currently an Assistant Professor at the Maersk Mc-Kinney Møller Institute, University of Southern Denmark. His research interests include surgical robotics, robot control, and machine learning.



Yuqiao Chen received the MEngSc degree in Biomedical Engineering from the University of New South Wales, Sydney, Australia, in 2018. He is currently pursuing a Ph.D. degree in Data Science at the City University of Macau. His research focuses on artificial intelligence and image pattern recognition algorithms in the field of medical robotics.



Bo Lu (Member, IEEE) received the PhD degree in mechanical engineering from The Hong Kong Polytechnic University, in 2019. He is currently an Associate Professor with the School of Mechanical and Electrical Engineering, Robotics and Microsystems Center, Soochow University, China. His current research interests include medical robotics, computer vision, and surgical automation techniques.



Wenjie Liu received the Master degree in the School of Electronic and Information Engineering from Tongji University, China in 2024. His current research interests include medical robotics, and continuum manipulator control.



Cesare Stefanini (Member, IEEE) received the M.Sc. degree (Hons.) in mechanical engineering and the Ph.D. degree (Hons.) in microengineering from Scuola Superiore Sant'Anna (SSSA), Pisa, Italy, in 1997 and 2002, respectively. He is currently a professor and the Director of BioRobotics Institute, SSSA. His research activity is applied to different fields, including underwater robotics, bioinspired systems, biomechatronics, and micromechatronics for medical applications.



Peng Qi (Member, IEEE) received the PhD degree in robotics from King's College London, U.K., in February 2016. He was a research fellow with the National University of Singapore, from 2015 to 2016, and a visiting scholar (honored) with The Chinese University of Hong Kong, from September 2016 to February 2017. He is currently an associate professor of robotics with Tongji University. His research interests include medical robotics, continuum manipulator, intelligent sensing and interaction.